2011

ADAPTIVE REFINEMENT AND MULTISCALE MODELING IN 2D PERIDYNAMICS

Florin Bobaru
University of Nebraska-Lincoln, fbobaru2@unl.edu

Youn Doh Ha
Kunsan National University, Korea

Journal for Multiscale Computational Engineering, 9 (6): 635–659 (2011)

ADAPTIVE REFINEMENT AND MULTISCALE MODELING IN 2D PERIDYNAMICS

***Florin Bobaru*[1,*] *& Youn Doh Ha*[1,2]**

[1]*Department of Mechanical and Materials Engineering, University of Nebraska-Lincoln, Lincoln, Nebraska 68588-0526, USA*

[2]*Assistant Professor, Department of Naval Architecture, Kunsan National University, Korea*

[*]Address all correspondence to Florin Bobaru, E-mail: fbobaru2@unl.edu

The original peridynamics formulation uses a constant nonlocal region, the horizon, over the entire domain. We propose here adaptive refinement algorithms for the bond-based peridynamic model for solving statics problems in two dimensions that involve a variable horizon size. Adaptive refinement is an essential ingredient in concurrent multiscale modeling, and in peridynamics changing the horizon is directly related to multiscale modeling. We do not use any special conditions for the "coupling" of the large and small horizon regions, in contrast with other multiscale coupling methods like atomistic-to-continuum coupling, which require special conditions at the interface to eliminate ghost forces in equilibrium problems. We formulate, and implement in two dimensions, the peridynamic theory with a variable horizon size and we show convergence results (to the solutions of problems solved via the classical partial differential equations theories of solid mechanics in the limit of the horizon going to zero) for a number of test cases. Our refinement is triggered by the value of the nonlocal strain energy density. We apply the boundary conditions in a manner similar to the way these conditions are enforced in, for example, the finite-element method, only on the nodes on the boundary. This, in addition to the peridynamic material being effectively "softer" near the boundary (the so-called "skin effect") leads to strain energy concentration zones on the loaded boundaries. Because of this, refinement is also triggered around the loaded boundaries, in contrast to what happens in, for example, adaptive finite-element methods.

KEY WORDS: *peridynamics, nonlocal methods, adaptive refinement, multiscale models, elasticity*

1. INTRODUCTION AND LITERATURE REVIEW

1.1 Introduction

In this paper we present and test a procedure for adaptive refinement in the numerical formulation of the peridynamics in two dimensions. Peridynamics is a nonlocal method that was introduced by Silling (2000) and generalized in a so-called state-based formulation by Silling et al. (2007). Here, we use the so-called "bond-based" peridynamics (Silling, 2000). The principles and algorithms developed here for the bond-based peridynamics can be easily modified to apply to the state-based formulation as well. As discussed by Bobaru et al. (2009), adaptivity in peridynamics is closely related to multiscale modeling because it is not only the grid spacing that changes but also the horizon size. The peridynamic horizon is one critical nonlocal parameter that introduces a length scale in the model, and when a variable horizon is used over a domain we effectively employ a multiple scales model.

While the main idea contained in this paper is a direct extension of the approach proposed for one dimension by Bobaru et al. (2009), a series of new algorithms specific to the higher dimensions are proposed and specific issues that pertain to the higher dimensions are addressed and treated in detail. For the quasi-static examples shown here no special interface conditions are needed. In dynamic problems such conditions are required and this will be reported in future work.

1543–1649/11/$35.00

The motivation for developing nonlocal methods comes from the fact that local methods, when applied to problems where localization phenomena and microstructural effects are involved (as in the case of crack propagation and crack branching, strain softening and shear bands formation, damage, etc.), suffer from convergence problems and mesh sensitivity. Local methods cannot capture size effects observed in fracture and damage of composite laminates, concrete, etc. To address these issues, a number of nonlocal methods have been proposed (for a recent review see, e.g., Bažant and Jirasek, 2002) over the years. Nonlocal methods attempt to capture the "effective" properties due to the microstructural details that are taken into account only approximately or indirectly. The material behavior is characterized by the material microstructure in direct connection with the applied loading (dynamic or quasi-static), the initial and boundary conditions, and the geometry of the sample. As pointed out by Bažant and Jirasek (2002), the growth of a microcrack is not decided by the local stress and strain tensors at the continuum point corresponding to the crack tip but by the overall energy release from a finite volume surrounding the entire microcrack. It is natural to also expect that when other cracks, defects, and/or inhomogeneities are present around the microcrack, the size of the volume mentioned above changes. Under certain conditions, especially in problems involving some type of damage, the actual microstructure and heterogeneities of the material are reflected in the observed material response. An example is the four-point bending tests for mixed-mode crack propagation in mortar and concrete (Arrea and Ingraffea, 1982). The experimentally observed crack paths correlate well with the particle size of the aggregates. Ways of measuring material length parameters have been reviewed, for example, by Bažant and Jirasek (2002). It is interesting to note that, in general, materials can exhibit various material length scales, depending on loading rates, boundary conditions, geometry, and microstructure (Abu Al-Rub and Voyiadjis, 2004; Voyiadjis and Abu Al-Rub, 2005).

The material microstructure and hierarchical architecture also appear to be a factor that leads to fault tolerance at different length scales (Yao and Gao, 2007). An interesting viewpoint on this topic is presented by Yao and Gao (2007), who showed that hierarchically structured materials, in contrast to conventional non-hierarchical materials, exhibit multi-scale cohesive laws that enable flaw insensitivity at all relevant size scales.

Classical theories fail to predict the material response in these cases where the microstructure plays a critical role. Using nonlocal methods, capturing size effects in the material response and numerical convergence for localization problems becomes possible (Bažant and Jirasek, 2002). Peridynamics is ideally suited for tackling such difficult problems, and especially those that involve discontinuous fields, such as discontinuous displacements across cracks. In applying peridynamics, gains in efficiency can be made if a variable horizon can be used. The peridynamic "horizon" is the effective region of nonlocal interaction around a material point. The motivation for the adaptive refinement algorithms developed here is twofold: (a) to gain efficiency compared with uniform refinement (in problems where length scales do not manifest explicitly) and (b) to offer seamless concurrent multiscale modeling of materials. Note that adaptivity in peridynamics can cover both continuum-to-continuum multiscale coupling and discrete-to-continuum coupling. In this paper we focus on the continuum-to-continuum multiscale coupling. In peridynamics, "continuum" is a nonlocal model of a continuum. For a discrete-to-continuum coupling in peridynamics, one needs to also change the structure of the micropotential, in addition to the change in horizon size (see Section 2 for the definitions). Some recent concurrent multiscale models (e.g., Tadmor et al., 1996; Miller and Tadmor, 2002; Belytschko and Xiao, 2003; Chamoin et al., 2010) have been trying to couple, for example, an atomistic (nonlocal) model to a classical continuum (local) model, to understand the mechanical behavior of materials at the micro- and nanoscales. These types of methods join together mathematically distinct models that result in "ghost" or spurious forces that disturb the equilibrium at the interface between the models. Special conditions then are enforced to resolve this problem; for example, corrections added as dead loads to the interface region (see Shenoy et al., 1999), Lagrange multiplier method in the bridging domain method (Belytschko and Xiao, 2003), and dead loads obtained by the Arlequin approach (Chamoin et al., 2010). We shall see that in the adaptive peridynamics there is no need to correct equilibrium at the interface between different horizon regions and the reason is because the transition is continuum-to-continuum and not discrete-to-continuum like in the other concurrent multiscale methods mentioned above.

The connection between grid refinement and multiscale methods is emphasized by Bažant (2010), where remarks are made about the care one has to use when employing multiscale methods for modeling of softening damage.

The original version of peridynamics uses a constant horizon over the domain. Due to the nonlocality (the horizon size), wave propagation in peridynamics, for example, is dispersive even in one dimension (see, e.g., Silling et al., 2003). The dispersion, however, decreases as the horizon goes to zero (see Xie, 2005; Bobaru et al., 2009) and

convergence to the classical elasticity solutions is obtained (Emmrich and Weckner, 2007; Silling and Lehoucq, 2008; Bobaru et al., 2009). Adaptive refinement in the meshfree numerical model for peridynamics (for the meshfree model, see Silling and Askari, 2005) involves reducing the size of the horizon together with a refinement of the nodal volumes (grid refinement) in regions of interest. Changing the horizon induces, in turn, scaling of the micromodulus values (see Bobaru et al., 2009). Special care has to be paid over the region of overlap between nodes with large horizons and nodes with small horizons (see Bobaru et al., 2009). Adaptive refinement reduces the computational cost in problems where stress/strain concentrations occur, in wave propagation and crack propagation problems. For the example of a plate with a hole treated here, a fine grid and a small horizon (relative to the size of the hole) are needed only around the strain concentration regions, whereas away from it, a large horizon (and, thus, a coarser grid) can be used to reduce the computational effort. For wave propagation problems (to be treated in a separate paper), using a "large" horizon (relative to the wavelength) over the region where the wave propagates may induce too much dispersion. A small horizon region that "travels" with the wave can either reduce dispersion to negligible values or produce dispersions similar to that of the real material. Outside of this region a much larger horizon (and coarser grid) may be used.

1.2 Brief Literature Review

1.2.1 Adaptive Methods and Quadtree Structures

Adaptive refinement methods are developed to automatically change mesh resolution in order to improve the accuracy in regions where steep gradients happen. In concurrent multiscale methods, adaptive refinement algorithms are important ingredients used to determine where and when a small-scale model needs to be inserted in a larger-scale model and to provide the transition between scales. For the finite-element method (FEM), adaptive refinement methods have been pioneered by Babuska and Rheinboldt (1978). Error estimators for adaptive refinement have been introduced by Zienkiewicz and Zhu (1987). Adaptivity has been employed also for nonlocal damage models in brittle materials by Rodriguez-Ferran and Huerta (2000), Rodriguez-Ferran et al. (2004), and Patzak and Jirasek (2004). One of the most effective ways of implementing adaptive refinement strategies is via recursive decomposition using quadtrees in two dimensions or octrees in three dimensions. Quadtree data structures have been used in image processing by Hunter and Steiglitz (1979) and Samet (1982), and in computer graphics by Samet and Webber (1988a,b) for quite some time. The use of quadtrees in finite-element studies was introduced by Yerry and Shephard (1983). Adaptive methods based on quadtrees are also widely used in finite-volume methods for modeling fluids (see, e.g., van Dommelen and Rundensteiner, 1989; De Zeeuw and Powell, 1993; Becker et al., 1995).

When used for mesh refinement in the FEM, however, quadtree meshes lead to non-conforming finite elements due to level mismatches between adjacent elements, which results in the presence of so-called hanging nodes. Complicated algorithms and interpolation functions are needed to handle the presence of these hanging nodes. To improve efficiency, the number of hanging nodes over an element face is minimized by using *restricted quadtrees* (see Babuska and Rheinboldt, 1978; Yerry and Shephard, 1983; Greaves and Brothwick, 1999), where the maximum difference between the levels of refinement of adjacent elements cannot be more than 1. A further simplification of the algorithms for quadtree refinement in finite elements has been recently proposed by Tabarraei and Sukumar (2005), in which the meshfree basis functions (from the "natural-neighbor" method) are used on a reference element combined with an affine map to construct conforming approximations on quadtree meshes. The natural-neighbor functions, however, require the use of Voronoi cells and these are expensive to construct, especially in three dimensions. An adaptive method based on Voronoi cell structure for meshfree solutions has been proposed by Lu and Chen (2002).

1.2.2 Peridynamics and Other Nonlocal Methods

Peridynamics is a reformulation of the classical continuum mechanics equations that allows for a natural treatment of discontinuities in the solution by employing the concept of nonlocal interactions (Silling, 2000). Integration, rather than differentiation, is used to compute the total force–density acting on a certain material volume, and deformation gradients are not used in the formulation. This novel approach allows for easy and mathematically consistent modeling of crack and damage initiation and propagation in complex settings (see, e.g., Silling and Askari, 2005; Silling and Bobaru, 2005; Bobaru, 2007; Ha and Bobaru, 2010a).

Note that peridynamics differs from other nonlocal methods such as those described by Eringen (1987), Kunin (1982), and Rogula (1982), or those reviewed by Bažant and Jirasek (2002), for at least two fundamental reasons:

- The deformation gradient and strains (spatial derivatives of displacements) are not used in peridynamics. Other nonlocal methods average infinitesimal strains over the nonlocal region. Spatial derivatives of the displacement field become undefined when cracks (discontinuities) emerge, and this requires special treatment and algorithms for modeling of fracture.
- Damage is introduced in the peridynamic method at the microlevel as the peridynamic bonds between material points reach a failure criterion related to the material's fracture energy. Fracture surfaces result autonomously as a consequence of this definition and dealing with multiple interacting cracks of arbitrary shapes in complex geometries becomes as easy as dealing with a single straight crack. In this way, peridynamics integrates damage and fracture under a single model for material failure.

In the original peridynamic formulation (the bond-based version) the interaction between material points was via pairwise forces (Silling, 2000). This leads to material models with a fixed Poisson ratio (one-fourth in three dimensions and one-third in two dimensions). Ways to remove this restriction are given by Silling (2000) and in the more general formulation developed by Silling et al. (2007). From the point of view of adaptive refinement the limitation of the bond-based peridynamics to modeling materials with a preset Poisson ratio is inconsequential, and in this paper we use the bond-based version for simplicity. Applications of the peridynamic formulation have been published on crack propagation in three-dimensional (3D) solids (Silling and Askari, 2005; Parks et al., 2008), dynamic crack branching in brittle plates (Ha and Bobaru, 2010a), fracture of thin rubber-like membranes (Silling and Bobaru, 2005), spallation (Xie, 2005), phase transition (Dayal and Bhattacharya, 2006), damage in nanofiber networks (Bobaru, 2007), damage in laminated composites (Xu et al., 2008; Hu et al., 2010), and trans- and inter-granular fracture in polycrystalline ceramics (Askari et al., 2008).

The types of phenomena that can be modeled using the peridynamic concepts are not limited to mechanical problems. Silling and Bobaru (2005) and Bobaru (2007) used Lenard-Jones-type forces between nanofiber networks, in addition to elastic bonds used along the nanofibers, to analyze the strength and damage properties of nanofiber networks. A peridynamic formulation for transient heat transfer was proposed by Bobaru and Duangpanya (2010). Peridynamic models have been implemented in a code from Sandia National Laboratories, named EMU, authored by Dr. Silling. An implementation of peridynamics within the well-regarded molecular dynamics code, LAMMPS, from Sandia National Laboratories, has been developed by Dr. Parks and named PDLAMMPS.

1.3 Paper Organization

The paper is organized as follows: in Section 2 we review the peridynamic formulation for microelastic materials in two dimensions. In Section 3 we present the particular discretization used in this work and the algorithm used for spatial integration; In Section 4 we introduce the algorithms used for the adaptive refinement in peridynamics using quadtrees; Numerical examples for a plate and a plate with a hole are shown in Section 5. Section 6 presents convergence results for the plate with a hole case. Conclusions are gathered in Section 7.

2. THE PERIDYNAMIC FORMULATION FOR MICROELASTIC MATERIALS

The peridynamics equations of motion at a point $\mathbf{x}$ and time t are given by (Silling, 2000)

$$\rho\,\ddot{\mathbf{u}}\left(\mathbf{x},t\right)=\int_{H_{\mathbf{x}}}\mathbf{f}\left[\mathbf{u}\left(\mathbf{x}',t\right)-\mathbf{u}\left(\mathbf{x},t\right),\mathbf{x}'-\mathbf{x}\right]\mathbf{dx}'+\mathbf{b}\left(\mathbf{x},t\right), \tag{1}$$

where $\ddot{\mathbf{u}}$ is the acceleration vector field; $\mathbf{u}$ is the displacement vector field; $\mathbf{b}$ is a prescribed body force intensity; and ρ is mass density, respectively. Also, $\mathbf{f}$ is a pairwise force function in the peridynamic bond (pair) that connects two "neighboring" particles, $\mathbf{x}$ and $\mathbf{x}'$. The internal subregion of nonlocal interaction between points, $H_{\mathbf{x}}$ (see Fig. 1), is defined as

$$H_{\mathbf{x}}=\{\mathbf{x}'\in\Re_0:|\mathbf{x}-\mathbf{x}'|<\delta\} \tag{2}$$

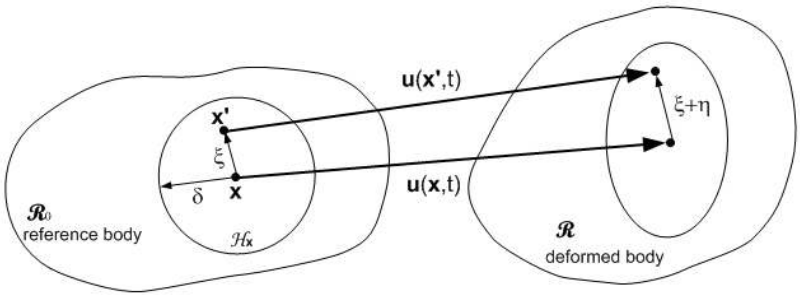

FIG. 1: The deformation of a peridynamic bond

where δ is the peridynamic horizon. We will use the name horizon for both region $H_{\mathbf{x}}$ and its radius. Note that no spatial derivatives appear in Eq. (1). The detailed formulation and relation to the conventional theory are given by Silling (2000). If the inertia effects can be neglected, the equilibrium equation is obtained:

$$\int_{H_{\mathbf{x}}} \mathbf{f}\left[\mathbf{u}\left(\mathbf{x}',t\right)-\mathbf{u}\left(\mathbf{x},t\right),\mathbf{x}'-\mathbf{x}\right]\mathbf{dx}'+\mathbf{b}\left(\mathbf{x},t\right)=\mathbf{0} \tag{3}$$

For a microelastic material (as defined by Silling, 2000), there exists a pairwise potential ω such that

$$\mathbf{f}\left(\eta,\xi\right)=\frac{\partial\omega\left(\eta,\xi\right)}{\partial\eta}\quad\forall\xi,\eta \tag{4}$$

where $\xi=\mathbf{x}'-\mathbf{x}$ is the relative position and $\eta=\mathbf{u}\left(\mathbf{x}',t\right)-\mathbf{u}\left(\mathbf{x},t\right)$ is the relative displacement (see Fig. 1). A linear microelastic material is defined by a micropotential ω as follows:

$$\omega\left(\eta,\xi\right)=\frac{c\left(\xi\right)s^2\left\|\xi\right\|}{2} \tag{5}$$

where $c\left(\xi\right)\xi$s the "micromodulus" function and

$$s=\frac{\left\|\eta+\xi\right\|-\left\|\xi\right\|}{\left\|\xi\right\|} \tag{6}$$

is the relative elongation of a bond. The corresponding pairwise force becomes

$$\mathbf{f}\left(\eta,\xi\right)=\frac{\partial\omega\left(\eta,\xi\right)}{\partial\eta}=c\left(\xi\right)s\left\|\xi\right\|\frac{\partial s}{\partial\eta}=c\left(\xi\right)s\frac{\partial\left\|\xi+\eta\right\|}{\partial\eta} \tag{7}$$

with

$$\frac{\partial\left\|\xi+\eta\right\|}{\partial\eta}=\frac{\xi+\eta}{\left\|\xi+\eta\right\|}=e \tag{8}$$

where e is the unit vector along the direction of the bond between $\mathbf{x}'$ and $\mathbf{x}$ in the deformed configuration $(\xi+\eta)$.

For a no-memory, isotropic, homogeneous, and microelastic material, the relations with a classical linear elastic material have been established by Silling and Askari (2005) for three dimensions; by Ha and Bobaru (2010a) for two dimensions; and by Bobaru et al. (2009) for one dimension. In this paper, we use the "constant" and "conical" micromoduli functions (see Fig. 2) with the plane stress assumption, which results in the two-dimensional (2D) constant micromodulus equal to:

$$c=\frac{6E}{\pi\delta^3\left(1-\nu\right)} \tag{9}$$

and the 2D conical micromodulus of

$$c\left(\xi\right)=\frac{24E}{\pi\delta^3\left(1-\nu\right)}\left(1-\frac{\left\|\xi\right\|}{\delta}\right) \tag{10}$$

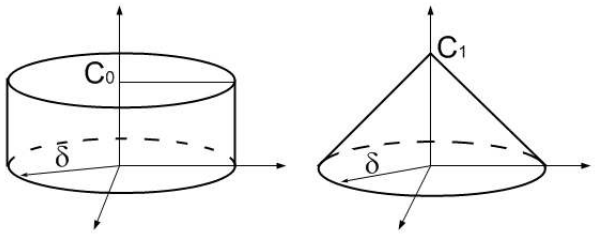

FIG. 2: Two examples of micromodulus functions: the constant micromodulus function (left) is discontinuous at the edge of the horizon; the conical micromodulus function (right), an example of a continuous micromodulus function

3. DISCRETIZATION AND TYPES OF CONVERGENCES

3.1 Discretization

To discretize the peridynamic equations we use the method described by Silling and Askari (2005) with a slightly different algorithm for the spatial integration. The body is discretized into a set of nodes, so that the sum of the nodal areas (nodal volumes in three dimensions) is the total area of the body.

The spatially discretized version of Eq. (1), at a node p, using a mid-point-type integration scheme is (other types of spatial integration may be used but they do not appear to bring any major benefits without interfering with the way damage and fracture are dealt with):

$$\rho\,\ddot{\mathbf{u}}\,(\mathbf{x},t) = \sum\nolimits_{q\in H_p} c\,(\|p-q\|)\,[\mathbf{u}\,(p,t)-\mathbf{u}\,(q,t)]\,A_{pq} + \mathbf{b}\,(p,t) \tag{11}$$

where A_{pq} is the portion of the area of node q covered by the horizon of node p.

The discretization needs not be uniform, although using uniform discretization is often more convenient from an implementation point of view. If the discretization is not uniform, the differences between the nodal volumes should not vary too much, unless special integration techniques are used to reduce the integration error caused by such changes in the grid.

In calculating the peridynamic bond force between nodes p and q in Eq. (11), it is necessary to calculate the portion of the area of node q covered by the horizon of the source node p. For example, in Fig. 3 the volume of

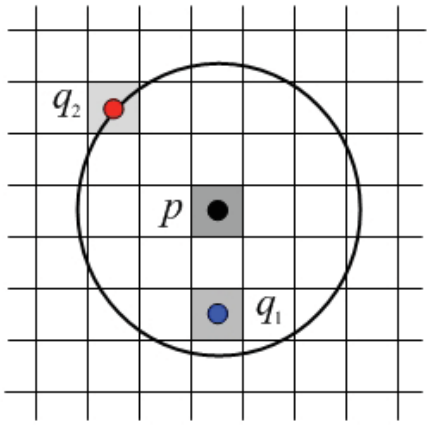

FIG. 3: The discretization of the domain. Node q_1 is fully covered by the horizon of node p, while node q_2 is only partially covered by the horizon of node p

node q_1 is completely covered by the horizon of source node p. However, the volume of node q_2 is only partially covered. One may not consider this volume as partially inserted and use the entire volume or, alternatively, drop it from the computation. This is simple, but it introduces numerical error. An accurate evaluation of the exact value of the partial area covered that is robust is not easy to develop, especially if the grid is not regular. Instead, we propose a simple, efficient, and robust algorithm (works also for irregular grids in which the nodal areas are quadrilaterals) that approximates the area in question. This algorithm can be easily extended to three dimensions. The algorithm (see Algorithm 1, where Δx, Δy are the grid spacings in the x, y directions, respectively) approximates the fraction of a nodal area partially covered by the horizon of the source node. Reasons for this particular choice of approximation are given in the report by Hu et al. (2011).

3.1.1 Algorithm 1: Partial area Approximation and Micromodulus Computation

1: **If** $\|\xi\| < \delta - \max(\Delta x, \Delta y)/2$

2: **Then** $\gamma = 1.0$

3: Compute micromodulus from Eq. (9) or Eq. (10) at $\|\xi\|$

4: **Else if** $\|\xi\| < \delta$

5: **Then** $\gamma = [\delta + \max(\Delta x, \Delta y)/2 - \|\xi\|] / \max(\Delta x, \Delta y)$

6: Compute micromodulus from Eq. (9) or Eq. (10) at $\|\xi\| - (1-\gamma)\max(\Delta x, \Delta y)/2$

7: **Else if** $\|\xi\| < \delta - \max(\Delta x, \Delta y)/2$

8: **Then** $\gamma = [\delta + \max(\Delta x, \Delta y)/2 - \|\xi\|] / \max(\Delta x, \Delta y)$

9: Compute micromodulus from Eq. (9) or Eq. (10) at $\delta - \gamma \max(\Delta x, \Delta y)/2$

10: **Else**

11: $\gamma = 0.0$

12: Micromodulus = 0.0

13: **End if**

3.2 Scaling for Grid Refinement

Adaptive refinement in peridynamics requires changes in the grid density and horizon. Changing the horizon induces changes in the micromodulus function [see Eq. (9) or (10)]. The process of changing the micromodulus when the horizon changes, is called scaling in peridynamics. This scaling in three dimensions was derived by Silling (2005) as

$$\omega_\varepsilon(\eta, \xi) = \gamma^3 \omega_\delta(\gamma\eta, \gamma\xi) \tag{12}$$

where ε is the "new" horizon, $\gamma = \delta/\varepsilon$. The 2D version of scaling is

$$\omega_\varepsilon(\eta, \xi) = \gamma^2 \omega_\delta(\gamma\eta, \gamma\xi) \tag{13}$$

It is easy to see that with this scaling relation, the elastic strain energy is kept constant as we change the horizon:

$$W_\delta(\mathbf{x}) = \frac{A}{2}\int_{H_\delta} \omega_\delta(\gamma\eta, \gamma\xi)\, d\left(\gamma^2 A\right) = \frac{A}{2}\int_{H_\varepsilon} \omega_\varepsilon(\eta, \xi)\, \gamma^2 dA = W_\varepsilon(\mathbf{x}) \tag{14}$$

Here, dA is the differential area.

4. QUADTREE REFINEMENT IN PERIDYNAMICS

4.1 Description of the Quadtree Structure Refinement in Peridynamics

Quadtrees in two dimensions (or octrees in three dimensions) are commonly used in adaptive refinement of grids because they guide the refinement process in a simple, fast, and efficient way. Quadtrees partition a 2D region by recursively subdividing it into four quadrants or sub-regions called "cells." The quadrilateral cell has four nodes and four edges (see Fig. 4). A node has adjacent cells and adjacent nodes. An adjacent cell to a node is a cell that contains the node in its list of nodes (we use the connectivity structure that gives, for each cell, the four nodes belonging to that cell). An adjacent node to a given node is one that is connected to it through an edge. Adjacent nodes are consecutive in the list of nodes of a cell (the last node in the list is "followed" by the first node since we implement circular lists). The new cells are called children of the decomposed (or parent) cell. A cell is called a leaf if it does not have any children. Two cells (which are leaves) are called neighboring or adjacent if they share an edge or a part of an edge. Each node has an index and we compare the node indices to see if any two cells are sharing their nodes. If it is true, those two cells are neighboring cells. The information about neighboring cells is used to search only around the neighbors of a current node, for finding hanging nodes (see below), and ultimately for computing the new nodal horizons and nodal areas after refinement. The *level* of a cell is the number of decompositions needed to reach that cell and this information is stored for each cell. The level of a *root* cell is set as zero (see Fig. 4). In Fig. 4 the spatial and logical representations of a quadtree are shown.

Non-uniform adaptive refinement using quadtrees leads to the so-called *hanging nodes* (see the red nodes in Fig. 4), which are the result of level mismatch between adjacent cells. These special nodes are the vertices of a smaller cell that lie on the edge of a larger cell and are not one of the larger cell's vertices. In the data structure we only create new nodes at the mid-points of a larger cell and at the center of that cell. To find the hanging nodes we use information from the neighboring cells. Using this information, we can loop over adjacent cells only, and if a new node is the mid-point of the edge of any neighboring cell then that node is a hanging node.

Various ways to deal with the presence of hanging nodes have been proposed over the years (see Section 1.2.1). In peridynamics, hanging nodes do not create any difficulties and important algorithmic simplifications can be achieved. These simplifications are possible because we use the "meshfree"-type discretization for peridynamics described above (Silling and Askari, 2005) that does not employ shape functions. Schemes for splitting the nodal areas (or nodal volumes in three dimensions) between the new and existing nodes need to be implemented. To that end, one option is to treat hanging nodes as any other node and have them participate in the area (or volume in three dimensions) splitting operation. The other option is to assign zero area (or volume in three dimensions) to the hanging nodes and thus eliminate them from the computation of the domain integral [see Eq. (11)]. The latter method requires that the area gets shared between the old nodes in the region of refinement and the newly inserted nodes that are not hanging nodes. In this work we use this second approach because it leads to a simpler algorithm.

Note that in this paper we do not consider coarsening (the opposite process to refinement) and we only perform one-stage refinement, meaning we do not use recursive algorithms to refine an already refined area. These two topics will be reported in future publications.

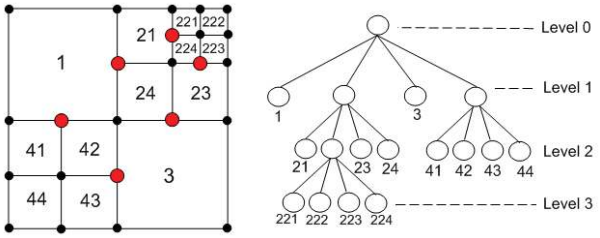

FIG. 4: The spatial and logical representation of a quadtree structure. Hanging nodes are present (red dots) at the interface between cells with different refinement levels.

4.2 Description of the Adaptive Refinement Process in Peridynamics

For adaptive refinement to take place, a triggering mechanism needs to be put in place. In classical models, like the FEM, error estimators have been developed (see, e.g., Zienkiewicz and Zhu, 1987) to trigger refinement of the mesh. In peridynamics we use the nodal strain energy to determine the regions where refinement needs to take place. In addition, we use the "visibility criterion" proposed by Bobaru et al. (2009), which requires the refinement area to be enlarged so that no node in the region that has been determined to be refined can be "seen" by a node from the coarse region. Effectively, this criterion refines also the nodes covered by the horizons of the nodes in the region to be refined.

The adaptive refinement process in peridynamics has the following structure: we first compute the nodal (nonlocal) strain energy density [by integrating Eq. (5) over the horizon at a node] and select a certain percentage of the maximum strain energy density (in the examples shown in this paper we use 40%). Nodes with at least that much strain energy density are part of the refinement region. Based on these nodes we determine the extra nodes to be refined due to the visibility criterion. A higher or lower percentage of the maximum strain energy density (say 50% or 30%) in the criterion for triggering adaptivity enlarges or shrinks the refined regions. The 40% value used here strikes a good balance between efficiency and solution accuracy.

After the set of nodes needed to be refined is determined, cells adjacent to one or more of these nodes are selected and refined. New nodes and cells are created and, consequently, the quadtree structure needs to be updated. Finally, the new nodal areas and nodal horizon sizes need to be calculated. These two procedures can be costly if they are performed through the entire grid, and using the information of neighboring cells, we could restrict these calculations to the region covering all cells that are adjacent to the nodes in the refinement area. In the current implementation, for simplicity, we perform the procedures over the entire grid.

The calculations for nodal areas and the nodal horizons for regular (with rectangular cells) or irregular grids (with general quadrilateral cells) are performed as described in Figs. 5 and 6. Observe that, due to the area splitting method described below and in Fig. 5, when adaptivity takes place, the mid-point spatial nodal integration of Eq. (1) will have reduced accuracy since some nodes are no longer in the middle of their domains. Consequently, convergence rates (for convergence to the exact nonlocal solution, if available) for adaptive refinement will be affected by this quadrature error, which is more pronounced near the transition zone between the refined and unrefined regions. In addition, this quadrature error may be responsible for the asymmetries discussed in Section 5. Exploration of more accurate integration over non-uniformly refined grids in peridynamics is a subject of future research.

4.2.1 Updating the Nodal Areas after Refinement

Figure 5 shows the procedure performed to compute the nodal areas for general 2D grids. The method is applicable for any grid represented by quad cells. The procedure can directly be extended to the 3D case. We first check if the

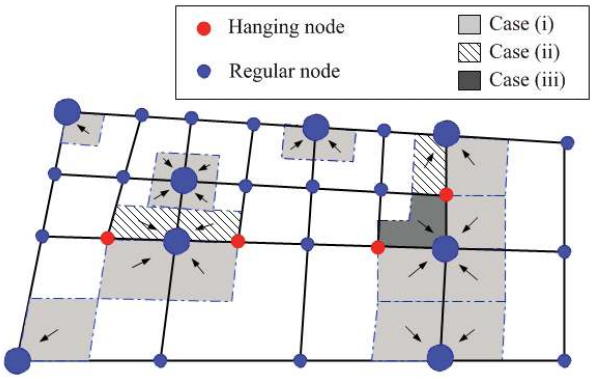

FIG. 5: Calculating nodal areas after refinement for a few nodes (depicted by the larger circles). The arrows indicate to which node the particular area belongs.

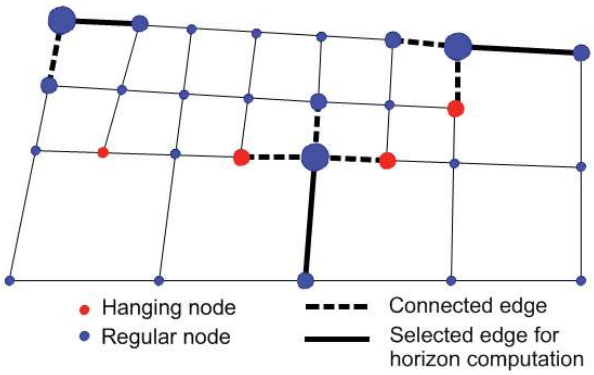

FIG. 6: Determination of the nodal horizons after refinement

current node is a hanging node. If it is, we assign zero area to it. Otherwise, we loop over all cells adjacent to this node and add a certain portion of the area of each adjacent cell to the nodal area. The area of a quad cell in the grid is computed by

$$A = \frac{1}{2}\sum_{i=1}^{4}\left(x_i y_{i+1} - y_i x_{i+1}\right) \tag{15}$$

where x_i and y_i are the coordinates in the reference configuration of cell's nodes and the node with local index 5 is identical to the node with local index 1 (we use circular lists). The portion of the adjacent cells' area assigned to the nodal area is based on the number of hanging nodes located in each of the adjacent cells and their *level* in the quadtree structure. To determine this, we first check if all adjacent cells to the current node have the same quadtree level (see Fig. 5). If they have, then one-quarter of each adjacent cell's area is added to the nodal area of the current node and the subroutine analyzes the next node. This is case (i) in Fig. 5. If the adjacent cells have different quadtree levels, then the number of hanging nodes contained by each of the adjacent cells is determined. In Fig. 5 we show the three possible cases (in two dimensions). The case when the adjacent cell has no hanging nodes among its corners is covered by case (i) above, so one-quarter of the area of the cell is added to the current node area. Case (ii) is when the adjacent cell has one hanging node among its corners. In this case, half of the cell area is added to the current node's area. Case (iii) occurs when an adjacent cell contains two hanging nodes among its vertices. In this case the portion of area added to the current node area equals three-quarters.

4.2.2 Updating the Horizon Information

The other procedure involved in the adaptive refinement in peridynamics is the horizon calculation. For nodes in the refined areas we also reduce the horizon so that parameter $m(x)$ (the ratio of the horizon of node x to the average grid spacing at x) has about the same value as in the coarse region. Note that if we did not change the horizon after refinement, the material model would not change, while when we change the horizon, a material with a different length scale is present.

The following strategy is used to update the horizons of nodes in the refined regions (see Fig. 6). We first build a list of nodes *adjacent* to a given node. Two nodes are adjacent if they share an edge in a cell. To determine if two nodes are adjacent we first obtain the list of adjacent cells to the node. We then analyze the list of nodes contained in each of the adjacent cells. Due to the connectivity structure, adjacent nodes to the given node are the nodes located to the left and right of the given node in the list. We use circular lists. If a node has more than one adjacent cell, the above analysis is performed for each adjacent cell; i.e., there is a different list of adjacent nodes for each adjacent cell. In the end, these lists are combined together into a final list of adjacent nodes, from which we eliminate repeated nodes. From this list, the maximum distance between the current node and its adjacent nodes is found. The maximum distance times a factor [close to the value of $m(x)$], defines the horizon, δ of the current node.

4.2.3 Remark

We implement adaptivity in peridynamics based on "restricted quadtrees," for which the maximum difference between the levels of refinement of adjacent cells cannot be more than 1. The reason for using the restricted quadtree in other methods is to reduce the number of hanging nodes. In peridynamics, we use the restricted quadtree structure simply to limit abrupt changes in the discretization level that could introduce larger numerical integration errors not because of the generation of hanging nodes.

5. PERIDYNAMICS WITH VARIABLE HORIZON

5.1 Transitioning between Horizons of Different Sizes

The refinement and adaptive refinement examples shown in this paper are for static problems. Dynamic problems in one dimension have been shown by Bobaru et al. (2009) and in two dimensions they will be reported in a future publication.

The original formulation of peridynamics (Silling, 2000) and the subsequent state-based formulation (Silling et al., 2007) are based on the implicit assumption that the horizon is constant over the domain. In this section we analyze in some detail the implications of using a non-constant horizon in peridynamics in two dimensions. The one-dimensional (1D) case has been discussed by Bobaru et al. (2009). Note that even in the constant horizon case, one can use a non-uniform grid of nodes for the integration of the equations of motion. However, the current mid-point spatial integration scheme that we use will introduce more numerical error than when all nodes are at the center of their corresponding volumes. The effect this numerical error has on the solutions will be visible in the numerical examples shown below.

When the horizon varies over the domain, some of the peridynamic bonds are "lost," in the following sense (shown schematically in Fig. 7): when we write the equation of motion at node p, there is a bond between node p and node q; however, when we reverse roles and write the equation of motion at node q, this time the bond between node q and node p does not exist anymore. This, however, does not contradict the equations of motion that are imposed at the nodes. In a sense, bonds can be viewed only as a means to compute the total force at a material point from that point's nonlocal continuum region. Note that in atomistic-to-continuum coupling (e.g., Tadmor et al., 1996; Miller and Tadmor, 2002; Belytschko and Xiao, 2003; Chamoin et al., 2010) ghost forces appear due to the discrete nature of the atomistic region. In our case, we transition from a nonlocal continuum to a nonlocal continuum, and ghost forces do not appear. However, when we discretize the nonlocal continua in our model, some spurious effects should be visible, but small enough that they can be neglected. In the numerical examples shown below we observe that the peridynamic solutions with a variable horizon (including solutions using adaptive refinement) converge to the classical, local model solutions in the limit of the horizon going to zero.

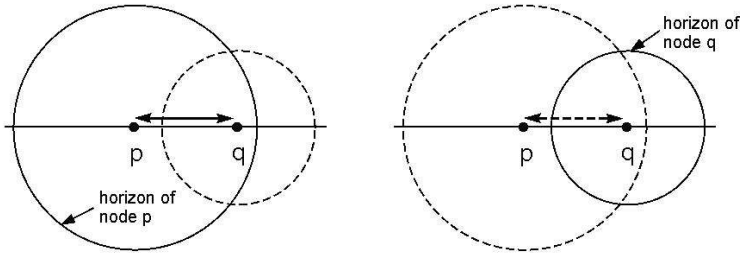

FIG. 7: Peridynamic bonds for the variable horizon case: the bond between nodes p and q exists when we write the equilibrium equation at p, but it does not exist when we write the equation at node q. The connection between these two points is now "mediated" by the continuum (points) within their corresponding horizons. No ghost forces result because of this, in contrast to what happens in concurrent discrete-to-continuum coupling models.

5.2 The Effect of the Boundary and of the Variable Horizon Size on the Peridynamic Solution

In this section we test the peridynamic solution with variable horizon for the quasi-static stretching of an elastic plate with and without a hole. We also analyze the influence of the localization effect induced by the micromodulus function on the variable horizon (including the case of refinement) solution when we use conical and a constant micromodulus functions.

We compare the peridynamic solutions with the classical elasticity solutions, computed here with a fine FEM (ABAQUS) mesh. Bobaru et al. (2009) introduced three types of numerical convergence for peridynamics. Here, we use the m-convergence concept with one small change. In the study done by Bobaru et al. (2009), m was the number of nodes inside the horizon. Here, we define m as the ratio of the horizon to the size of the local spatial discretization (for regular square grids):

$$m\left(\mathbf{x}\right) = \frac{\delta\left(\mathbf{x}\right)}{\Delta x} \tag{16}$$

This parameter no longer has to be an integer. Note that if an irregular grid is used, then instead of grid spacing Δx, a local average grid spacing should be used in the formula above. The advantage of the present formulation is that it is consistent for all dimensions.

We consider first a thin plate with dimensions of 6 cm $\times$ 6 cm subject to a traction q of 10 MPa applied [as shown in Fig. 8(a)]. The mid-points of the top and bottom edges are fixed in the x direction while the mid-points of the left and right edges are fixed in the y direction [see Fig. 8(a)]. This is not the minimal number of conditions for the classical, local formulation. However, in the peridynamic, nonlocal formulation, the minimal set of conditions needs to be enlarged compared to the local formulation (for a discussion of imposing boundary conditions in peridynamics, see Silling, 2000).

Microelastic models corresponding to a linear elastic material with Young's modulus of 1 GPa (and Poisson's ratio of 1/3) are used in all examples below. The classical solution for the stretched plate problem has constant strains and stresses. The maximum horizontal and vertical displacements for this problem are 0.3 mm and 0.1 mm, respectively.

In the first numerical model we use a regular (square) nodal structure with grid spacing of 1 mm and constant horizon (δ of 4 mm. The x and y displacements across the plate are shown in Fig. 8 for the two micromodulus functions, constant and conical [see Eqs. (9) and (10) and Fig. 2]. We notice that the peridynamic solutions feature a "skin effect," which is induced by an effectively "softer" material near the boundary due to the "missing" bonds for the nodes within a thickness δ from the boundary of the plate (see also Ha and Bobaru, 2010b). The skin effect is reduced when the micromodulus function is more localized, as is the case for the conical micromodulus. Indeed, the displacement fields obtained with the conical micromodulus in Figs. 8(b) and (d) are relatively uniform inside the bulk but not uniform near the boundaries due to the skin effect. The solutions obtained with the constant micromodulus show similar patterns but the non-uniformity of the solutions due to the skin effect is much larger than that obtained with the conical micromodulus [as seen from Figs. 8(c) and (e)].

Obviously, decreasing the horizon reduces the skin effect, as will be shown in Section 6. Note that it is possible to remove the skin effect if one changes the micromodulus function for nodes near the boundary. From an algorithmic point of view it is simpler to use the same micromodulus function everywhere. Note also that the skin effect at a certain scale (the atomic scale) is actually a physical phenomenon. In practical computations performed for macro-scale structures, using a small horizon (relative to the geometrical dimensions of the analyzed body) is sufficient to make the skin effect negligible.

We now consider the same setup as above but with a refined grid region [as shown in Fig. 9(a)]. The horizon and the grid spacing in the refined region are changed so that the horizon of a node inside the refined grid is half of the horizon in the coarse grid; therefore, $\delta = 2$ mm in the refined region. The grid is generated using the quadtree structure over a pre-set region and the grid spacing determines the horizon size (see Section 4). We also keep the horizon of a node on the interface between the initial and the refined grids the same as the initial horizon $\delta = 4$ mm (see Section 4). Note that nodes near and on the boundary between the refined and coarse regions are like those shown in Fig. 7.

The results in Fig. 9 show that there are no ghost forces produced at the interface between the two scales, the large and small horizon regions. However, the numerical integration error induces some small deviations from a perfectly symmetric solution—as seen from Figs. 9(b) and (d) for the displacement fields with the constant micromodulus and

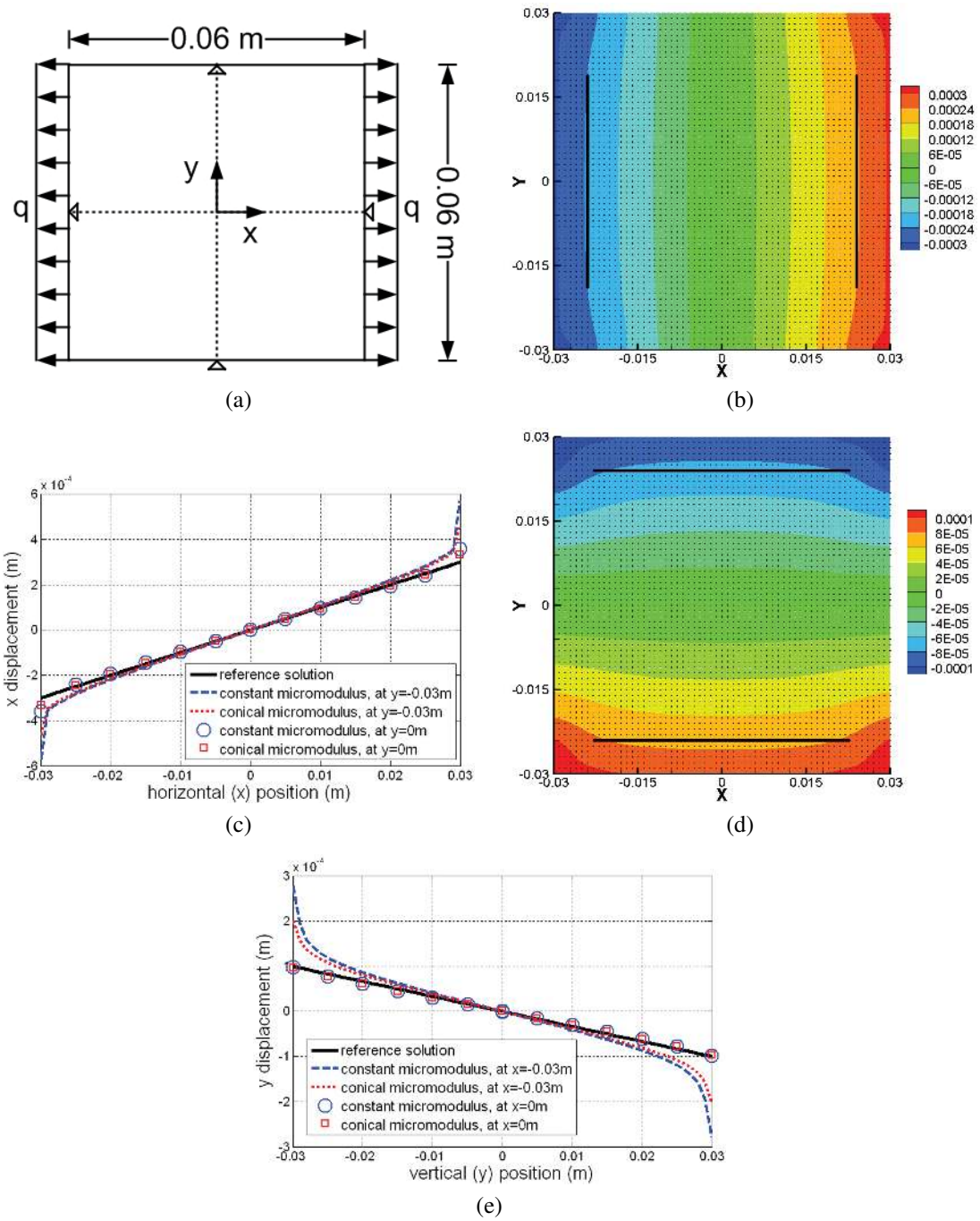

FIG. 8: **(a)** Plate model; **(b)** x displacement (conical); **(c)** x displacements for two micromoduli; **(d)** y displacement (conical); **(e)** y displacements for two micromoduli. The stretched plate model **(a)** and the peridynamic solutions for the x and y displacements with the conical micromodulus [in **(b)** and **(d)**, where solid lines are used to show the skin effect in the solution] and comparisons with the classical (the reference) solution [in **(c)** and **(e)** along horizontal lines at $y = 0$, and $y = -0.03$ m, and vertical lines at $x = 0$ and $x = -0.03$ m]. Here, $\delta = 4$ mm and $m = 4$.

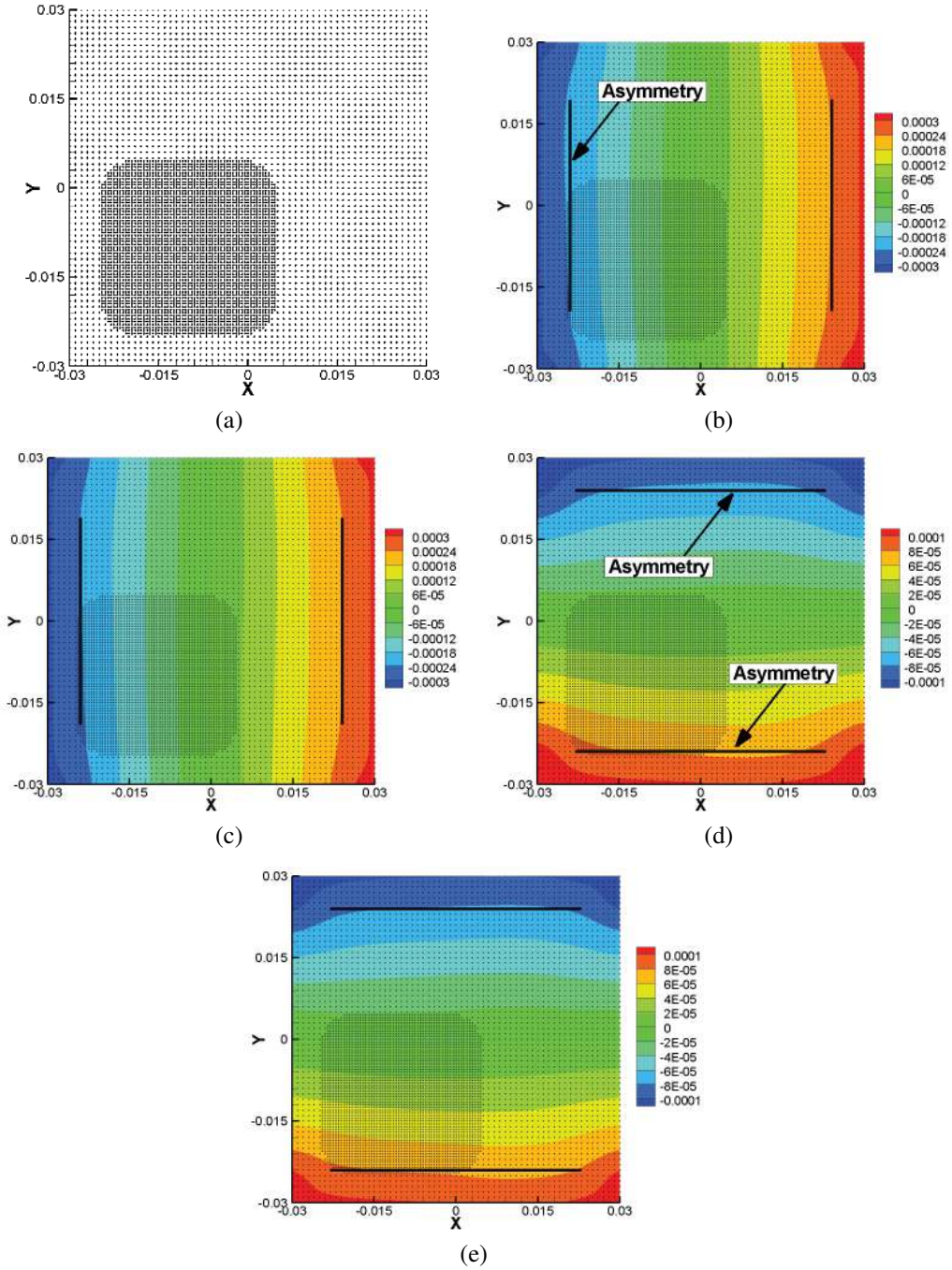

FIG. 9: **(a)** A pre-set refined region; **(b)** x displacement (constant micromodulus); **(c)** x displacement (conical micromodulus); **(d)** y displacement (constant micromodulus); **(e)** y displacement (conical micromodulus). Peridynamic solutions for the stretched plate problem over a grid with a refined region: **(b)**, **(d)** solutions with the constant micromodulus function, and **(c)**, **(e)** the conical micromodulus function. All grid nodes are plotted with a square of the same size to be able to easily identify the finer grid (smaller horizon) areas; solid lines are used to observe the small asymmetries in the solutions.

from Figs. 9(c) and (e) with the conical micromodulus function. This deviation disappears if the refinement region is placed in the center, matching the grid symmetry. As expected, the deviation from symmetry for the solution obtained with the conical micromodulus function shown in Figs. 9(c) and (e) is smaller than that obtained with the constant micromodulus function.

We next test the case of the plate with a hole for which we do not refine but the grid is non-uniform (see Fig. 10), and we generate the horizons based on this grid (see Section 4). The resulting horizons will, therefore, be variable and again there are nodes like those shown schematically in Fig. 7.

We consider a square thin plate with the hole [as shown in Fig. 10(a)]. The computational grid (generated with ABAQUS) is not uniform, especially around the hole; hence, the bond "asymmetry" discussed in Fig. 7 is prevalent for nodes near the hole. Note also that the grid structure near the hole is not symmetric about the center. We apply symmetric tensile loading conditions, this time enforced as prescribed horizontal displacements of $d = 0.4$ mm. For simplicity, we impose the displacements only over the boundary nodes and not over a layer of thickness δ inside the body (see Silling, 2000). The effect of this choice, together with the fact that we do not change the micromodulus function for nodes near the boundary to eliminate the skin effect, will be discussed in more detail in Section 6. The material properties are the same as for the plate without a hole. We compute the solution for the classical local problem by finite elements with a very fine grid (223,080 nodes, grid spacing ≈ 0.125 m). The x and y displacements are illustrated in Figs. 10(b) and (c). The maximum values of x and y displacements are 0.4 mm and about 0.15 mm, respectively. The peridynamic model is discretized using 3,675 nodes with an approximate nodal spacing of 1 mm. The horizon size is determined based on the grid structure (see Section 4), and it is 4 mm for nodes far from the hole and varies around this value for nodes near the hole. In Figs. 12(a) and (c), we observe that the displacements obtained with the constant micromodulus function present barely visible asymmetry (see the differences around the corners compared to the FEM results). The solution with the conical micromodulus is almost perfectly symmetrical, as can be seen from Figs. 12(b) and (d). Also, the skin effect is more pronounced with the constant micromodulus than with the conical one.

5.3 Decreasing of Horizon (δ)

As the horizon goes to zero, the peridynamic solution (with a constant horizon) converges to a corresponding local model solution (see, e.g., Silling and Lehoucq, 2008). We test this here, numerically, for the case of a variable horizon.

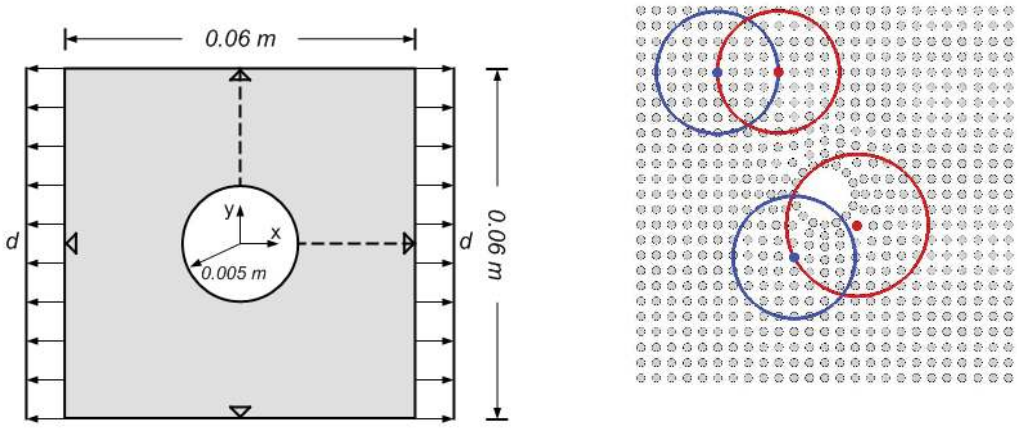

(a) (b)

FIG. 10: (a) Plate with hole problem; **(b)** non-uniform grid structure. The description of the stretching of a plate with a hole **(a)**; a sample non-uniform grid structure which leads to a variable horizon size **(b)**.

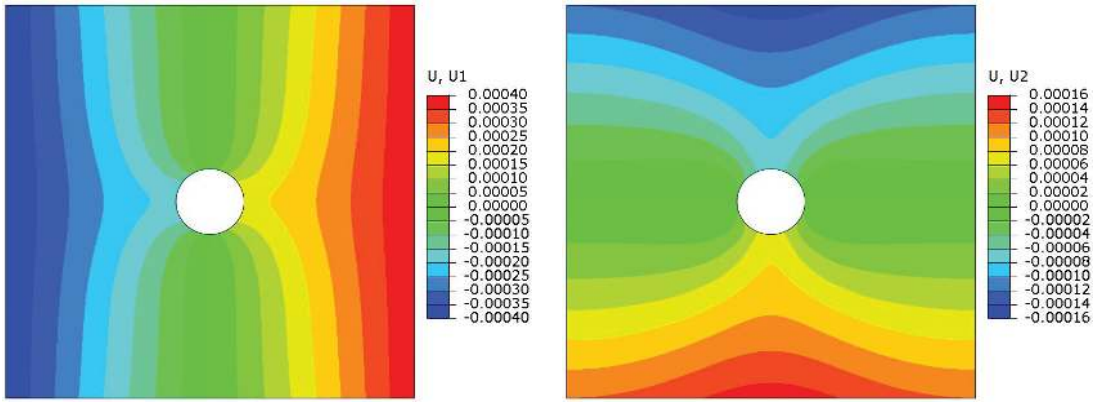

(a) (b)

FIG. 11: The finite-element solution (displacements) for the plate with a hole: **(a)** x displacement (FEM); **(b)** y displacement (FEM)

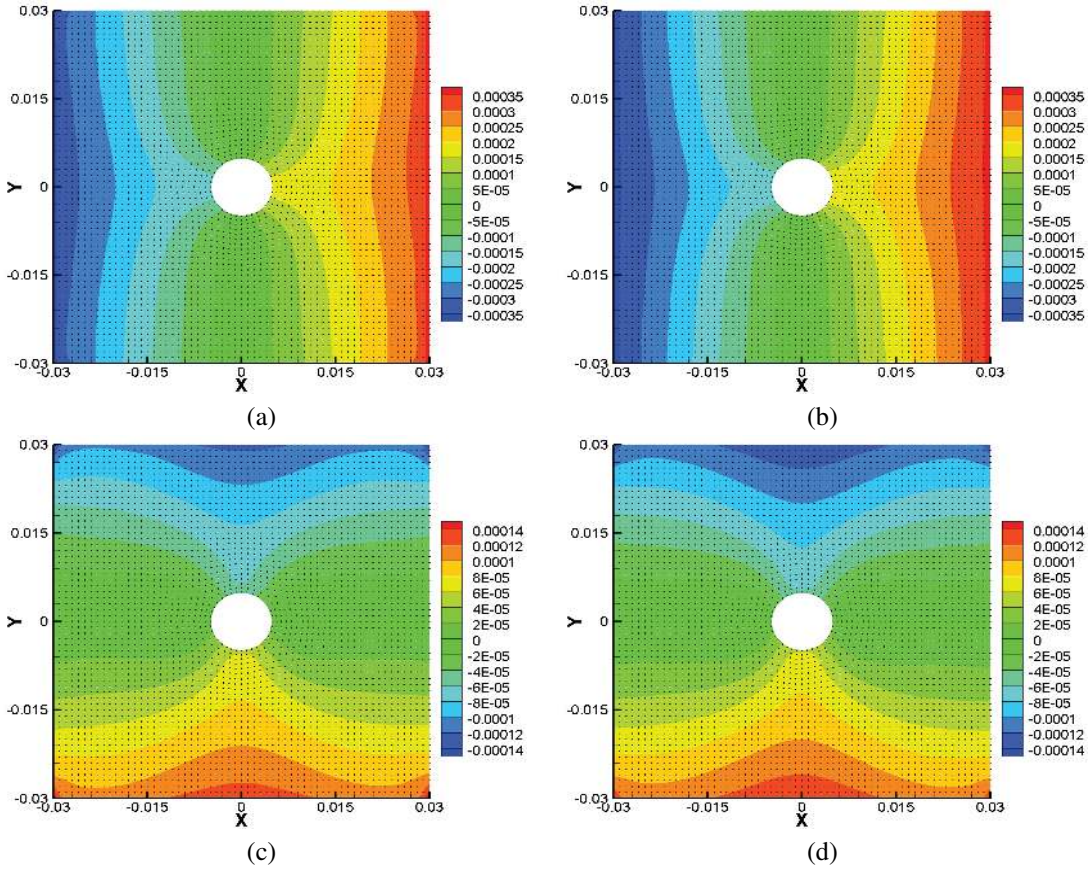

(a) (b)

(c) (d)

FIG. 12: Peridynamic displacements for the plate with a hole problem with two different micromodulus functions ($\delta \approx 4$ mm): **(a)** x displacement (constant micromodulus); **(b)** x displacement (conical micromodulus); **(c)** y displacement (constant micromodulus); **(d)** y displacement (conical micromodulus)

We consider the plate with a hole in Fig. 10(a) with the same conditions as above. The results from a finite element model obtained with a sufficiently fine mesh are shown in Fig. 11. In Fig. 13(a), the y displacement for the constant micromodulus case obtained with a horizon size is half of the one used for the solution in Fig. 12(b) (and using the same value for m). The skin effect is visible. When using about the same number of nodes (and the horizon corresponding to a value of $m = 4$) as the fine finite-element mesh that produced the results seen in Fig. 11, the peridynamic solution with the conical micromodulus [see Fig. 13(b)] is almost identical to the finite-element solution (see Fig. 11).

6. ADAPTIVITY AND CONVERGENCE STUDY FOR THE PLATE WITH A HOLE

In this section we compare the performance of uniform and adaptive refinement for the plate with the hole problem discussed above. Note that even for the uniform refinement case, due to the non-uniformity of the grid and the fact that we compute the horizons based on the grid (see Section 4), the horizon is not constant over the domain. In uniform refinement we decrease the grid spacing (at the boundaries) by half each time, and this leads to decreasing the horizon also by about half. In adaptive refinement, only certain regions have their grids and horizons changed, most of the area stays with the original (coarse) grid and a (relatively) large horizon. For all computations in this section we use the conical micromodulus function.

6.1 Uniform Refinement

For the convergence study in the uniform refinement, we perform the δ-convergence tests for four different horizon sizes: $\delta \sim 4$, 2, 1, and 0.5 mm. For all models the number of nodes inside a horizon (for nodes in the bulk) is around 50. We analyze the same problem of the plate with the hole seen in Fig. 10(a). The horizon is not constant over the domain and varies most around the hole where the grid is highly non-uniform. We compare the x displacements along the central horizontal line [see the horizontal dotted line in Fig. 10(a)] obtained with these different peridynamic models in Fig. 14(a). The comparison for the y displacements along the central vertical line [see the vertical dotted line in Fig. 10(a)] is shown in Fig. 14(b). The "exact" or reference solution is the solution for the classical, local model, obtained with a fine finite-element grid. The displacements obtained with peridynamics approach the reference solutions as the horizon decreases. Due to the skin effect, x displacements near the right edge (at $x = 3$ cm) differ more from the local solution, as expected. Note that the right edge ($x = 3$ cm) carries external loadings (the prescribed

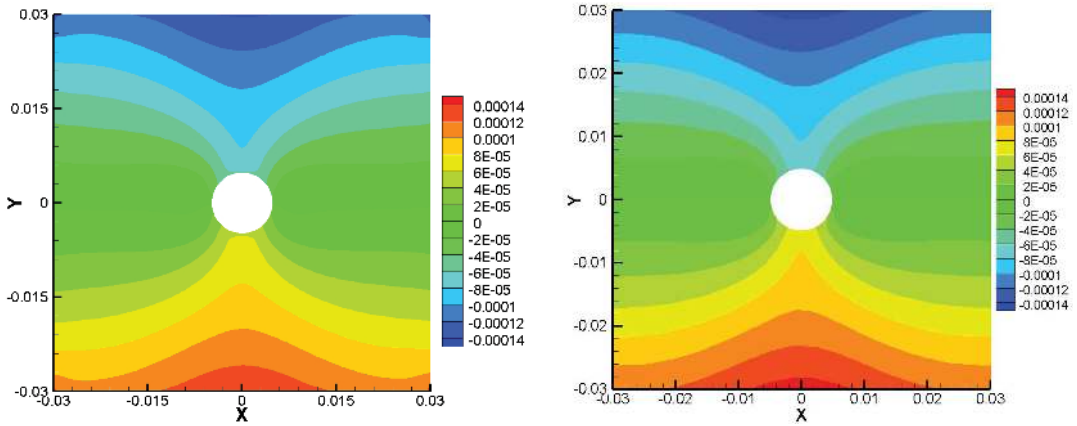

(a) (b)

FIG. 13: Peridynamic solutions (y displacements) with smaller horizons: **(a)** $\delta \approx 2$ mm, constant micro-modulus; **(b)** $\delta \approx 0.5$ mm, conical micromodulus. Compare with the results from the local model obtained with finite elements in Fig. 11.

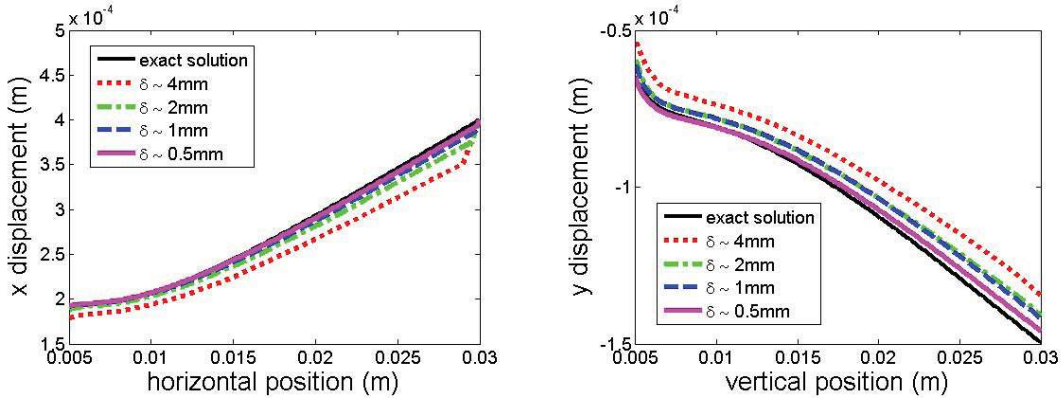

FIG. 14: Solution behaviors with uniform refinement (δ-convergence tests): **(a)** x displacement on the central horizon; **(b)** y displacement on the central vertical

displacements are imposed only on the boundary nodes). Clearly, the skin effect reduces as the horizon decreases.

6.2 Selecting the Adaptive Refinement Regions

Holes in loaded structures induce stress concentrations around them. For the plate with the hole problem above, the stress/strain concentrations take place around the top and bottom areas of the hole. These regions are candidates for adaptive refinement. In the present implementation in which the skin effect is present (we do not do anything special for nodes within a distance δ from the boundary), when displacement is imposed on the boundary nodes, an additional area of stress concentration is produced. This happens because having the same form of the micromodulus function for all nodes in the discretization results in an effectively softer material in a region of thickness δ at the boundary, which is progressively softer the closer to the boundary we get. Therefore, the strains will be larger for the "skin" regions on boundaries where displacements or tractions are imposed. The schematic for this behavior is shown in Fig. 15. For comparison, we also draw the behavior of the classical (local) material under the same conditions. The behavior of the peridynamic solution shown in Fig. 14 in comparison with the classical local solution can now be better understood. We use the algorithm described in Section 4 to automatically determine the regions for refinement. Figure 16 shows a sample result of using this algorithm for the stretching of the plate with a hole.

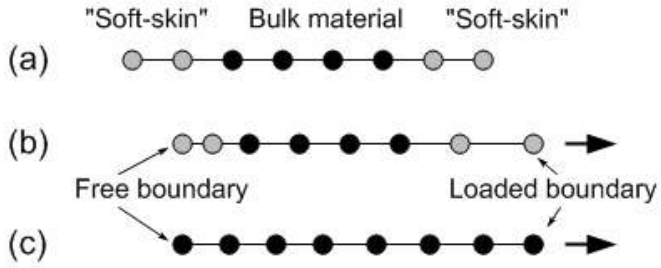

FIG. 15: Schematic of the influence of the skin effect on deformation along the horizontal dotted line in Fig. 10: **(a)** Peridynamic material before the deformation; **(b)** after the deformation. Notice that the boundary region on the loaded boundary deforms more than the bulk. The free boundary region shrinks a little. **(c)** The classical (local model) material after deformation.

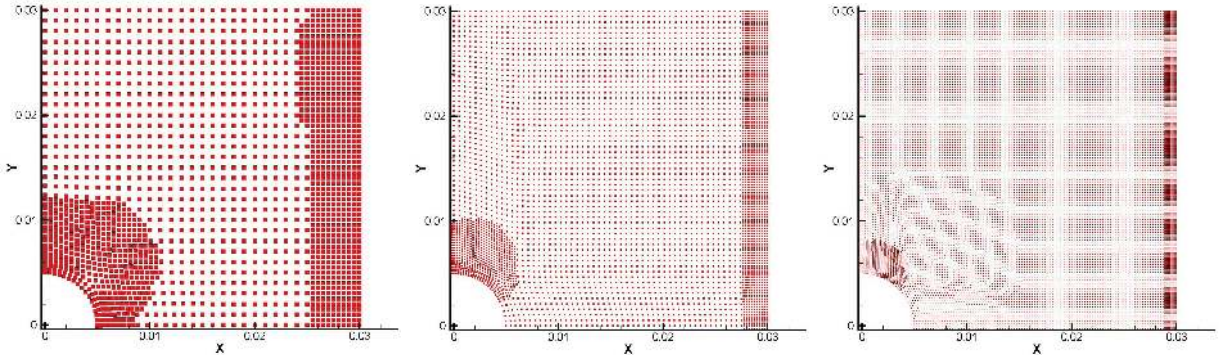

FIG. 16: Adaptive refinement grid for three different horizon models: in the coarse regions the horizon sizes are 4 mm, 2 mm, and 1 mm, from the left figure to the right, respectively, and in the refined region the horizon is 2 mm, 1 mm, and 0.5 mm. Only a quarter of nodal structure is shown.

We next investigate the influence of the adaptive refinement regions on the solution; for example, we see what happens if we only refine around the hole since for a local, classical model only that region would trigger refinement. We start with a model for the plate with a hole that has a horizon of about 4 mm (corresponding to a grid with an average grid spacing of 1 mm). We choose three types of refinement strategies: refining only near the loading boundary (Case A), only near the hole (Case B), or both near the loading boundary and the hole (Case C). Since the grid spacing in the refined grid is half of the one in the initial uniform grid, the horizon in the refined grid is also half of the initial horizon (e.g., δ is 4 mm in the unrefined region and is 2 mm in the refined region). The horizon of a node in the transition region between the unrefined and refined zones is the same with the horizon in the unrefined region. Other choices for the transition zone are possible (see Bobaru et al., 2009). In addition, we also use the "visibility criterion" discussed by Bobaru et al. (2009) for the 1D case, which enlarges the refinement region to cover not only the nodes in the region of refinement but also all of the nodes (therefore, cells) that are within a distance δ from such nodes.

In Fig. 17, the x and y displacements, near the hole and in the vicinity of the boundary where displacements are imposed, are compared between the three adaptive refinement cases discussed above, the local (FEM) solution, and the base, coarse "uniform" grid peridynamic solution.

- Case A: If we refine only near the loaded boundary, the displacements near the hole are not much different from those obtained by the local model (FEM). However, the slopes of these displacements, which are related to the strains, are more similar to the slopes for the solution obtained with the non-refined, coarse, peridynamic solution. Clearly, this refinement strategy is not beneficial in getting a better approximation of the stress/strain concentration around the hole. Nevertheless, the refinement near the loaded boundary reduces the skin effect compared with the non-refined solution.

- Case B: When only the region near the hole is refined, the slopes of the displacements near the hole are close to those given by the local solution. However, this strategy does not reduce the skin effect, and this causes the displacements to still be rather far from the classical ones.

- Case C: We clearly benefit most if we allow the area of high strain energy near the hole and those near the loading boundaries to be refined.

6.3 Performance of the Adaptive Refinement under Δ-Convergence

We now analyze the convergence behavior of the adaptively refined versions of the four numerical models used in Section 6.1. Case C (see previous section) is used here. As the starting grid (horizon) gets smaller, the area of adaptive

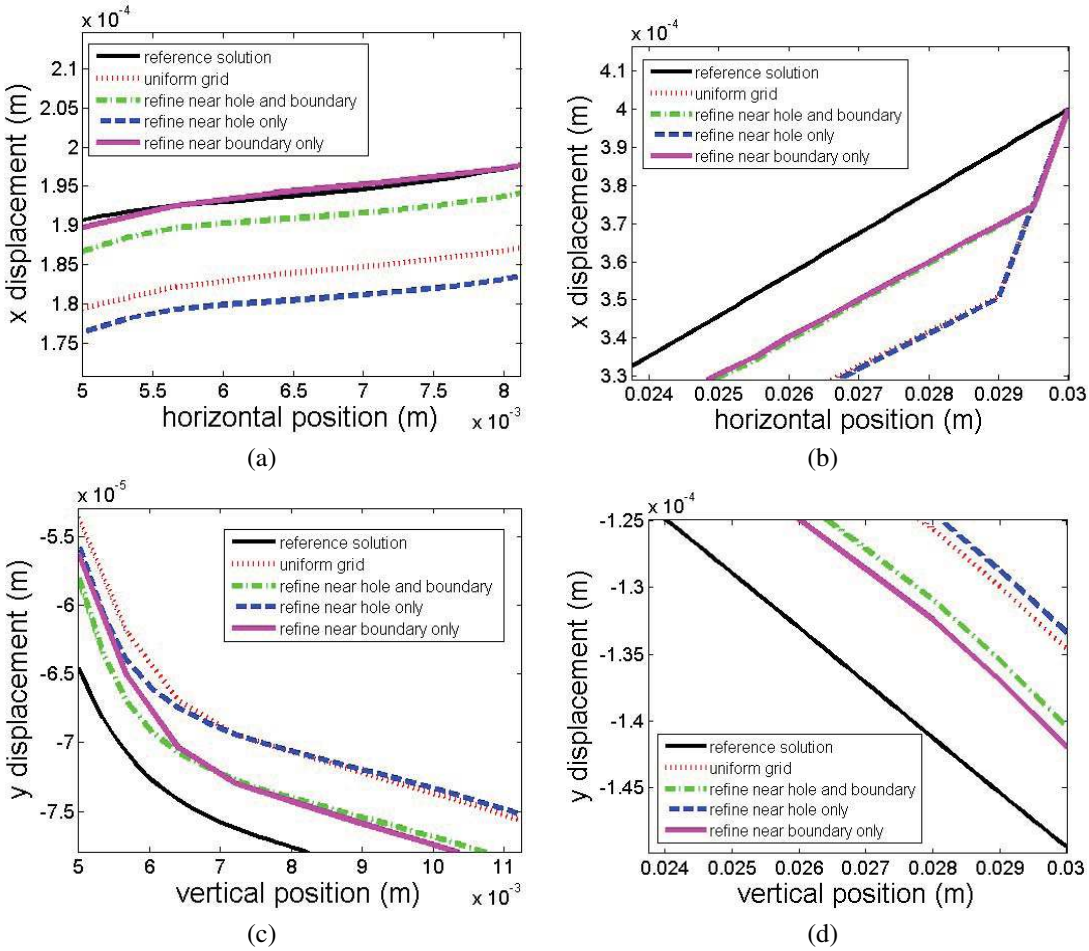

FIG. 17: Comparisons of solutions obtained with the three different adaptive refinement cases, the peridynamic coarse "uniform" grid, and the finite-element method (the "reference" solution): **(a)** x displacement for points near the hole; **(b)** x displacement near the left boundary; **(c)** y displacement for points near the hole; **(d)** y displacement near the left boundary

refinement decreases, too. This happens because of the stress concentration and the design of the algorithm that triggers the adaptivity discussed in Section 4. Along the central horizontal and vertical central lines of the plate seen as the dotted lines in Fig. 10(a), we compare the x and y displacements for the four different models in Figs. 18(a) and (b), respectively. In the legend of Fig. 18, we give the values of the horizon in the initial (coarse) and refined regions, for each model. The "exact" solution is again the solution obtained with a fine finite-element mesh. The displacements show convergence behavior as the horizon decreases. The influence of the "skin" is also observed.

In Fig. 19, the convergence behavior against the local solution for displacements obtained using peridynamics with uniform and adaptive refinements is shown. To measure the difference from the classical solution we use the norm-2 average "error" per node:

$$L_2 \text{ error} = \frac{1}{n}\frac{\left\|\mathbf{u}^{\text{numerical}} - \mathbf{u}^{\text{reference}}\right\|}{\left\|\mathbf{u}^{\text{reference}}\right\|} = \frac{1}{n}\frac{\sqrt{\sum_{i=1}^{n}\left(u_i^{\text{numerical}} - u_i^{\text{reference}}\right)^2}}{\sqrt{\sum_{i=1}^{n}\left(u_i^{\text{reference}}\right)^2}} \tag{17}$$

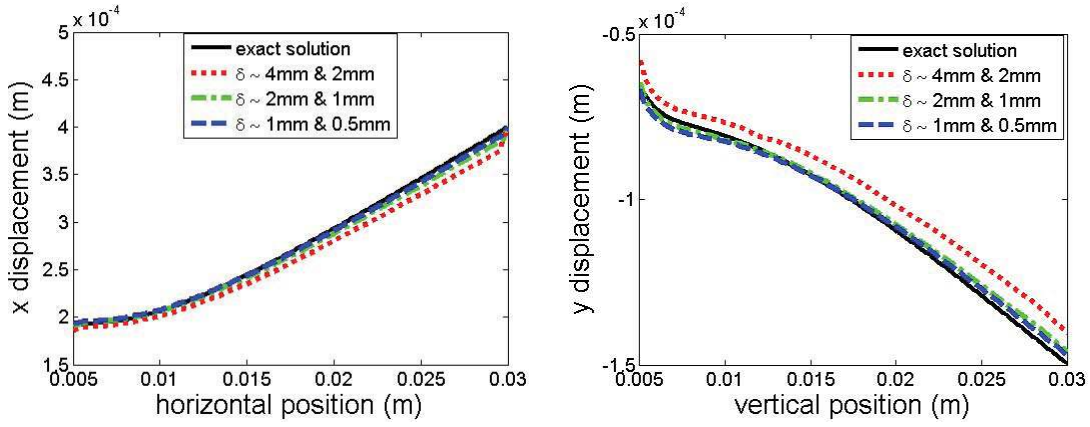

(a) (b)

FIG. 18: Comparison between the classical local solution and the peridynamic adaptively refined solutions with several decreasing horizons (δ-convergence test): **(a)** x displacement along horizontal dotted line in Fig. 10; **(b)** y displacement along the vertical dotted line in Fig. 10

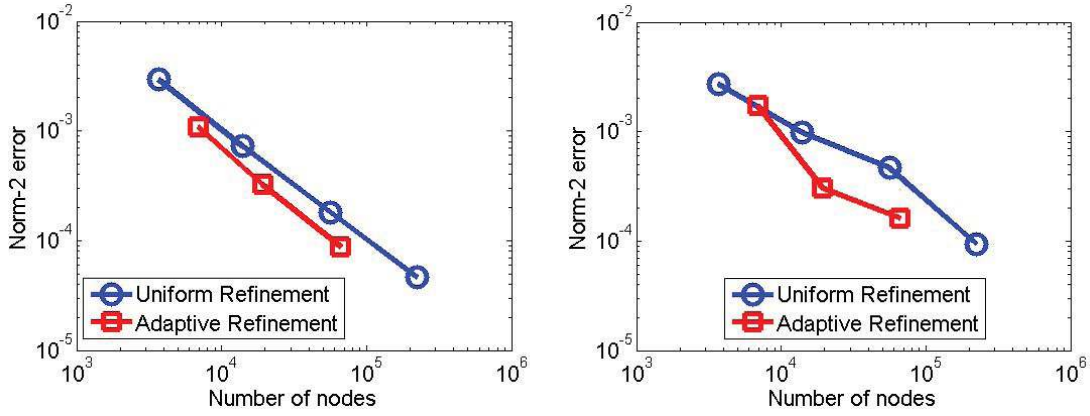

(a) (b)

FIG. 19: Relative difference from the local model solution for peridynamic models under uniform and adaptive refinements (log-log plot) (norm-2 average nodal error versus the total number of nodes): **(a)** x displacement; **(b)** y displacement

where n is the total number of nodes in a model. The peridynamic displacement $u^{\text{numerical}}$, which can be the x or y displacements, is compared with the reference solution ($u^{\text{reference}}$) from the finite-element analysis of the corresponding local model with very fine grid [seen in Figs. 10(b) and (c)]. As expected, the adaptively refined solution leads to a lower norm-2 error than the solution with uniform grids for the same number of nodes. In order to obtain the similar difference from the classical solution, a solution with an adaptively refined grid uses several times fewer nodes than the number of nodes of the solution based on the "uniform" grid.

More importantly, the stress concentration area is resolved more efficiently with adaptive refinement. We compare strains at point P (see Fig. 20) above the hole (of radius 5 mm and with its center at the center of the coordinate system), with coordinates $x = 0$ mm and $y = 6.036$ mm given by the finite-element grid that produced the reference solution. We chose this point because it is close to the stress concentration region and is not in the skin region if the

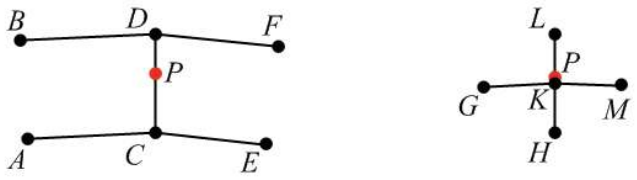

FIG. 20: Schematic diagrams of nodes in the grid for the 1 mm horizon nearby point P of coordinates (0, 6.036 mm) and the 0.5 mm horizon region in the refined case (see Tables 1 and 2)

horizon is less than 0.5 mm. However, even if the horizon is 0.5 mm, this node still "sees" (covers with its horizon) nodes in the skin region. The skin effect discussed before will influence the peridynamic results relative to the classical ones. For a horizon slightly larger than 0.5 mm the node is in the skin region. The finite-element solution (using bilinear elements) for the strains is: $\varepsilon_{xx} = 2.474 \times 10^{-2}$ and $\varepsilon_{yy} = -4.612 \times 10^{-3}$. We point out that these values are not the exact solution, but they are probably less than 1% different from it. The finite-element solution with biquadratic elements gives $\varepsilon_{xx} = 2.472 \times 10^{-2}$ and $\varepsilon_{yy} = -4.597 \times 10^{-3}$. We compare the strains at P with those obtained from the peridynamic solution using a 1 mm horizon with and without adaptivity. The refinement regions for the adaptive case are shown in the last graph in Fig. 16. In Table 1 we give the coordinates and the displacements at the nodes in the 1 mm horizon grid that are nearby point P.

We use the peridynamic nodal displacements to approximate the strains at this location P based on finite-difference approximations and linear interpolation to the selected point. Note that we could use shape functions to compute strains and stresses from the nodal displacements, at least for the regions where there are no hanging nodes. The approximation for ε_{xx} at P using the peridynamic displacement results is as follows: use forward finite difference at C (using value E) to get e_1 and backward finite difference at C (using value at A) to get e_2; get e_3, the horizontal strain as C, as the average between e_1 and e_2. Repeat a similar process with data at B, D, and F to compute e_6, the average horizontal strain at D. Use linear interpolation through the strain data points e_1 and e_6 to obtain the approximation for the horizontal strain at P. We obtain the value 2.511×10^{-2}. For the solution with adaptive refinement (see the last plot in Fig. 16) the value can be obtained at point P a little more directly because the point is very near a node in the grid. Using the data in Table 2 we get for the horizontal strain 2.489×10^{-2}. This value is less than 1% different from the classical one. The increase in the number of nodes compared with the unrefined solution is less than 20%.

For the strain along the vertical direction at point P the values from the finite-element solution are given above. Using a forward difference approximation based on the vertical displacements of nodes C and D we get -4.766×10^{-3} from the coarse solution with a horizon of 1 mm. From the solution with an adaptively refined horizon (and grid), using central difference between nodes H and L (see Fig. 20) we obtain -4.561×10^{-3}.

7. CONCLUSIONS

In this paper we introduced adaptive refinement for peridynamics in two dimensions for seamless multiscale modeling. The original peridynamics is formulated for a constant horizon throughout the domain. We show here how the

TABLE 1: Coordinates and peridynamic displacements at nodes shown in Fig. 20 (left picture)

Nodes shown in Fig. 20	***x* coordinate (m)**	***y* coordinate (m)**	u_x(m)	u_y(m)
A	-2.523×10^{-4}	5.879×10^{-3}	-6.411×10^{-6}	-7.002×10^{-5}
B	-2.528×10^{-4}	6.106×10^{-3}	-5.928×10^{-6}	-7.111×10^{-5}
C	0.0	5.893×10^{-3}	2.396×10^{-7}	-7.022×10^{-5}
D	0.0	6.120×10^{-3}	2.288×10^{-6}	-7.131×10^{-5}
E	2.517×10^{-4}	5.875×10^{-3}	6.885×10^{-6}	-6.997×10^{-5}
F	2.524×10^{-4}	6.103×10^{-3}	6.382×10^{-6}	-7.107×10^{-5}

TABLE 2: Coordinates and peridynamic displacements for nodes shown in Fig. 20 (right picture)

Nodes shown in Fig. 20	*x* coordinate (m)	*y* coordinate (m)	u_x(m)	u_y(m)
G	-1.263×10^{-4}	6.000×10^{-3}	-2.932×10^{-6}	-7.558×10^{-5}
H	0.0	5.893×10^{-3}	2.142×10^{-7}	-7.510×10^{-5}
K	0.0	6.006×10^{-3}	2.098×10^{-7}	-7.565×10^{-5}
L	0.0	6.120×10^{-3}	2.054×10^{-7}	-7.614×10^{-5}
M	1.260×10^{-4}	5.998×10^{-3}	3.348×10^{-6}	-7.555×10^{-5}

formulation can be directly extended to cover solutions with a non-constant horizon. We discuss several examples that show a seamless transition between the different sizes of the horizon is possible and no special techniques are required to couple the different scales: the large horizon regions to small horizon regions. No ghost forces result at the transition between the different scales (horizons), in contrast to what happens in concurrent discrete-to-continuum coupling models. The difference is attributed to the nonlocal continuum-to-nonlocal continuum coupling in peridynamics. Due to the dispersive nature of the peridynamic solutions induced by the nonlocality, in dynamic problems (to be discussed in a future work) conditions need to be imposed at the transition region to avoid reflections due to impedance mismatch. For the static problems shown here no extra conditions are necessary, in contrast with other concurrent multiscale methods.

We verify the correctness of our solutions against the classical, local model solutions by taking the horizon to zero. Adaptive refinement algorithms based on quadtree structures are simple to use with peridynamics and the presence of hanging nodes does not become an issue here since we use the meshfree-type discretization of the peridynamic equations. While we link the horizon size to the grid spacing so that, on average, each node covers with its horizon about the same number of nodes, the purpose is not to have the refinement process driven by the grid spacing but by the horizon size. In the examples shown, for comparison with the classical, local solutions, we took the horizon to smaller and smaller values. In problems where material length scales are present, the horizon size in the refinement regions would have to be associated with that material length scale while outside a larger horizon (and, therefore, a coarser grid) can be used.

The method and algorithms proposed here allow us to compute accurately stress concentration zones, which are potential regions of damage initiation. The approach developed in this paper will be used in the future to model crack propagation with increased efficiency and represents a key first step in developing peridynamic multiscale models.

ACKNOWLEDGMENTS

This work has been supported by grants from the Sandia National Laboratories (project manager Dr. S. A. Silling), the Boeing Company (project manager Dr. E. Askari), and the ARO/ARL (program managers Dr. Bruce LaMattina, and Dr. Chian-Fong Yen). Dr. Mijia Yang and Mr. Leonardo Alves have helped with an earlier version of the implementation used here.

REFERENCES

Abu Al-Rub, R. K. and Voyiadjis, G. Z., Analytical and experimental determination of the material intrinsic length scale of strain gradient plasticity theory from micro- and nano-indentation experiments, *Int. J. Plast.*, vol. **20**, pp. 1139–1182, 2004.

Arrea, M. and Ingraffea, A. R., Mixed-mode crack propagation in mortar and concrete, *Technical Report 81-13*, Cornell University, Ithaca, NY, 1982.

Askari, E., Bobaru, F., Lehoucq, R. B., Parks, M. L., Silling, S. A., and Weckner, O., Peridynamics for multiscale materials modeling, *J. Phys.: Conf. Ser.*, vol. **125**, pp. 1–11, 2008.

Babuska, I. and Rheinboldt, W. C., A posteriori error estimates for the finite element method, *Int. J. Numer. Methods Eng.*, vol. **1**, no. 12, pp. 1597–1615, 1978.

Bažant, Z. P., Can multiscale-multiphysics methods predict softening damage and structural failure? *Int. J. Multiscale Comp. Eng.*, vol. **8**, no. 1, pp. 61–67, 2010.

Bažant, Z. P. and Jirasek, M., Nonlocal integral formulations of plasticity and damage: Survey of progress, *J. Eng. Mech.*, vol. **128**, no. 11, pp. 1119–1149, 2002.

Becker, R., Johnson, C., and Rannacher, R., Adaptive error control for multigrid finite element methods, *Computing*, vol. **55**, pp. 271–288, 1995.

Belytschko, T. and Xiao, S. P., Coupling methods for continuum model with molecular model, *Int. J. Multiscale Comp. Eng.*, vol. **1**, no. 1, pp. 115–126, 2003.

Bobaru, F., Influence of van der Waals forces on increasing the strength and toughness in dynamic fracture of nanofiber networks: a peridynamic approach, *Modell. Simul. Mater. Sci. Eng.*, vol. **15**, pp. 397–417, 2007.

Bobaru, F. and Duangpanya, M., The peridynamic formulation for transient heat conduction, *Int. J. Heat Mass Transfer*, vol. **53**, no. 19-20, pp. 4047–4059, 2010.

Bobaru, F., Yang, M., Alves, L. F., Silling, S. A., Askari, E., and Xu, J., Convergence, adaptive refinement, and scaling in 1D peridynamics, *Int. J. Numer. Methods Eng*., vol. **77**, pp. 852–877, 2009.

Chamoin, L., Prudhomme, S., Ben Dhia, H., and Oden, T., Ghost forces and spurious effects in atomic-to-continuum coupling methods by the Arlequin approach, *Int. J. Numer. Methods Eng.*, vol. **83**, no. 8–9, pp. 1081–1113, 2010.

Dayal, K. and Bhattacharya, K., The kinetics of phase boundaries in the peridynamic formulation of continuum mechanics, *J. Mech. Phys. Solids*, vol. **54**, pp. 1811–1842, 2006.

De Zeeuw, D. and Powell, K. G., An adaptively refined Cartesian mesh solver for the Euler equations, *J. Comput. Phys.*, vol. **104**, pp. 56–68, 1993.

Emmrich, E. and Weckner, O., On the well-posedness of the linear peridynamic model and its convergence towards the Navier equation of linear elasticity, *Commun. Math. Sci.*, vol. **5**, no. 4, pp. 851–864, 2007.

Eringen, A. C., Theory of nonlocal elasticity and some applications, *Res. Mech.*, vol. **21**, pp. 313–342, 1987.

Greaves, D. M. and Brothwick, A. G. L., Hierarchical tree-based finite element mesh generation, *Int. J. Numer. Methods Eng.*, vol. **45**, pp. 447–471, 1999.

Ha, Y. D. and Bobaru, F., Studies of dynamic crack propagation and crack branching with peridynamics, *Int. J. Fract.*, vol. **162**, no. 1-2, pp. 229–244, 2010a.

Ha, Y. D. and Bobaru, F., Characteristics of dynamic brittle fracture captured with peridynamics, *Eng. Fract. Mech.*, vol. **78**, no. 6, pp. 1156–1168, 2010b.

Hu, W., Ha, Y. D., and Bobaru, F., Numerical integration in peridynamics, *Technical Report*, Department of Engineering Mechanics, University of Nebraska-Lincoln, 2010.

Hu, W., Ha, Y. D., and Bobaru, F., Modeling dynamic fracture and damage in fiber-reinforced composites with peridynamics, *Int. J. Multiscale Comp. Eng.*, vol. **9**, no. 6, pp. xx–xx, 2011.

Hunter, G. M. and Steiglitz, K., Operations on images using quadtree, *IEEE Trans. Pattern Anal. Mach. Intell.*, vol. **1**, pp. 145–153, 1979.

Kunin, I. A., *Elastic Media with Microstructure. I: One-Dimensional Models*, 1st ed., Berlin: Springer, 1982.

Lu, H. and Chen, J. S., Adaptive meshfree particle method, *Lect. Notes Comput. Sci. Eng*., vol. **26**, pp. 251–267, 2002.

Miller, R. E. and Tadmor, E. B., The quasicontinuum method: Overview, applications and current directions, *J. Comput.-Aided Mater. Des.*, vol. **9**, pp. 203–239, 2002.

Parks, M. L., Lehoucq, R. B., Plimpton, S. J., and Silling, S. A., Implementing peridynamics within a molecular dynamics code, *Comput. Phys. Commun.*, vol. **179**, no. 11, pp. 777–783, 2008.

Patzak, B., and Jirasek, M., Adaptive resolution of localized damage in quasi-brittle materials, *J. Eng. Mech.*, vol. **130**, no. 6, pp. 720–732, 2004.

Rodriguez-Ferran, A. and Huerta, A., Error estimation and adaptivity for nonlocal damage models, *Int. J. Solids Struct.*, vol. **37**, no. 48–50, pp. 7501–7528, 2000.

Rodriguez-Ferran, A., Morata, I., and Huerta, A., Efficient and reliable nonlocal damage models, *Comput. Methods Appl. Mech. Eng.*, vol. **193**, no. 30–32, pp. 3431–3455, 2004.

Rogula, D., *Nonlocal Theory of Material Media*, 1st ed., Berlin: Springer, 1982.

Samet, H., Neighbor finding techniques for images represented by quadtrees, *Comput. Graph. Image Process.*, vol. **18**, pp. 37–57, 1982.

Samet, H. and Webber, R. E., Hierarchical data structures and algorithms for computer graphics, I. Fundamentals, *IEEE Comput. Graph. Appl.*, vol. **8**, no. 3, pp. 48–68, 1988a.

Samet, H. and Webber, R. E., Hierarchical data structures and algorithms for computer graphics, II. Applications, *IEEE Comput. Graph. Appl.*, vol. **8**, no. 4, pp. 59–75, 1988b.

Shenoy, V. B., Miller, R., Tadmor, E. B., Rodney, D., Phillips, R., and Ortiz, M., An adaptive finite element approach to atomic-scale mechanics—the quasicontinuum method, *J. Mech. Phys. Solids*, vol. **47**, no. 3, pp. 611–642, 1999.

Silling, S. A., Reformulation of elasticity theory for discontinuities and long-range forces, *J. Mech. Phys. Solids*, vol. **48**, pp. 175–209, 2000.

Silling, S. A., Homogenization and scaling of peridynamic material models, *Unpublished Report*, 2005.

Silling, S. A. and Askari, E., A meshfree method based on the peridynamic model of solid mechanics, *Comput. Struct.*, vol. **83**, no. 17-18, pp. 1526–1535, 2005.

Silling, S. A. and Bobaru, F., Peridynamic modeling of membranes and fibers, *Int. J. Non-Linear Mech.*, vol. **40**, no. 2-3, pp. 395–409, 2005.

Silling, S. A. and Lehoucq, R. B., Convergence of peridynamics to classical elasticity theory, *J. Elast.*, vol. **93**, pp. 13–37, 2008.

Silling, S. A., Zimmermann, M., and Abeyaratne, R., Deformation of a peridynamic bar, *J. Elast.*, vol. **73**, pp. 173–190, 2003.

Silling, S. A., Epton, M., Weckner, O., Xu, J., and Askari, E., Peridynamic states and constitutive modeling, *J. Elast.*, vol. **88**, pp. 151–184, 2007.

Tabarraei, A. and Sukumar, N., Adaptive computations on conforming quadtree meshes, *Finite Elem. Anal. Design*, vol. **41**, pp. 686–702, 2005.

Tadmor, E. B., Ortiz, M., and Phillips, R., Quasicontinuum analysis of defects in solids, *Philos. Mag. A*, vol. **73**, no. 6, pp. 1529–1563, 1996.

van Dommelen, L. and Rundensteiner, E. A., Adaptive summation of point forces in the two-dimensional Poisson equation, *J. Comput. Phys.*, vol. **83**, pp. 126–147, 1989.

Voyiadjis, G. Z. and Abu Al-Rub, R. K., Gradient plasticity theory with a variable length scale parameter, *Int. J. Solids Struct.*, vol. **42**, pp. 3998–4029, 2005.

Xie, W., Peridynamic flux-corrected transport algorithm for shock wave studies, *Master's Thesis*, Department of Engineering Mechanics, University of Nebraska-Lincoln, Lincoln, Nebraska, 2005.

Xu, J., Askari, E., Weckner, O., and Silling, S. A., Peridynamic analysis of impact damage in composite laminates, *J. Aerosp. Eng.*, vol. **21**, no. 3, pp. 187–194, 2008.

Yao, H. and Gao, H., Multi-scale cohesive laws in hierarchical materials, *Int. J. Solids Struct.*, vol. **44**, pp. 8177–8193, 2007.

Yerry, M. and Shephard, M., A modified-quadtree approach to finite element mesh generation, *IEEE Comput. Graphics Appl.*, vol. **3**, no. 1, pp. 39–46, 1983.

Zienkiewicz, O. C. and Zhu, J. Z., A simple error estimator and adaptive procedure for practical engineering analysis, *Int. J. Numer. Methods Eng.*, vol. **24**, no. 2, pp. 337–357, 1987.